Planar Task Space Control of a Biarticular Manipulator Driven by Spiral Motors

Regular Paper

Ahmad Zaki bin Hj Shukor[1] and Yasutaka Fujimoto[1,*]

1 Department of Electrical and Computer Engineering, Yokohama National University
* Corresponding author E-mail: fujimoto@ynu.ac.jp

Abstract This paper elaborates upon a musculoskeletal-inspired robot manipulator using a prototype of the spiral motor developed in our laboratory. The spiral motors represent the antagonistic muscles due to the high forward/backward drivability without any gears or mechanisms. Modelling of the biarticular structure with spiral motor dynamics was presented and simulations were carried out to compare two control methods, Inverse Kinematics (IK) and direct-Cartesian control, between monoarticular only structures and biarticular structures using the spiral motor. The results show the feasibility of the control, especially in maintaining air gaps within the spiral motor.

Keywords biarticular manipulator, inverse kinematics control, work space control, spiral motor, musculoskeletal

1. Introduction

Over recent decades robots have been inspired by the motion of living things, i.e., humans and animals [1] [2]. Various structures of robots have been designed, from industrial robotic manipulators to humanoids and mobile legged robots for different purposes. Success stories include ASIMO, DLR, Big Dog and many others. However, most designs are implemented by using serial joint servos at the end of each limb, resulting in large joint actuators at the base to support the desired large forces/torques (i.e., end-effector output, friction). In the end, the weight and size of the actuators contribute largely to the overall specification of the robot. In addition, difficulties in actuation, for example, backlash and low drivability/low compliance, add to problems in controlling such structures.

On the other hand, the anatomy of the musculoskeletal human body provides new insights into the design of robots. By looking closely at the structure of the human/animal musculoskeleton, the joint/hinges are not directly actuated, but affected by the antagonistic contraction or extension of the muscles connected to the bones. The muscles can be clustered into monoarticulars (single joint articulated) and biarticulars (two joint actuated). The dynamic domain of the human arm muscles (from shoulder to elbow) have been studied in [3] [4] [5]. The study in [3] applies the Hill's muscle model and attempted to analyse different damping and elastic properties, and later applied task position feedback control to monitor position, velocity and accelerations in

joint and taskspace. On the variation of muscle positioning, the potential fields produced by the internal forces are affected and also the speed of convergence of motion. By means of simulation, the human reaching movements were achieved without inverse dynamics or optimal trajectory derivation.

Some designs that include biarticular muscle actuation can be referred to in [6] and [7]. These designs use rotary motors, belts and pulleys to realize biarticular muscle torques. In [6], stiffness and inverse dynamics feedforward control was applied. The lancelet (ancestor of the vertebrae) has inspired [7] using similar mechanisms to realize a virtual triarticular sigmoid/swimming motion with the properties of AC motor control. These designs include the biarticular/triarticular actuation, but the structures are maintained as serial or open-link mechanisms. Another different design was shown in [8], whereby the rotary motors are placed at the base and the joint angles are pulled by wires. Feedforward control was also applied to resolve force redundancy. Other designs of legged musculoskeletal mechanisms can be found in [9] [10] [11]. These structures utilize the pneumatic rubber muscles as actuators, possibly the closest candidate to the human muscle. These muscles extend or contract, depending on the amount of air pressure supplied. The small size of the actuators enables the design of the legs to be space saving, as the actuators are placed closely or attached to the link. Jumping and hopping motions were successfully implemented, but because of the use of air supply, these structures are less mobile for autonomous operations. Also, pneumatic muscles are difficult to control and inaccurate due to their nonlinear elasticity properties [12]. A combination of pneumatics/cables is also shown in [13].

The actuator that we propose for musculoskeletal actuation is the spiral motor [14]. It is a novel high thrust force actuator with high forward/backdrivability. From the first prototype, the internal permanent version was developed and currently the helical surface permanent magnet prototype is available [15].

2. Biarticular Manipulator Kinematics

An example of the biarticular muscle structure can be found in the human arm, consisting of antagonistic pairs of monoarticular (muscles affecting one joint) and biarticular muscles (muscles affecting two joints). By using the spiral motor, the antagonistic pair of flexor and extensor can be combined by using only one spiral motor, thus reducing the number of actuators from the shoulder to the elbow to only three actuators, instead of six. The combined flexor/extensor muscles of the planar manipulator of the biarticular structure is shown in Figure 1.
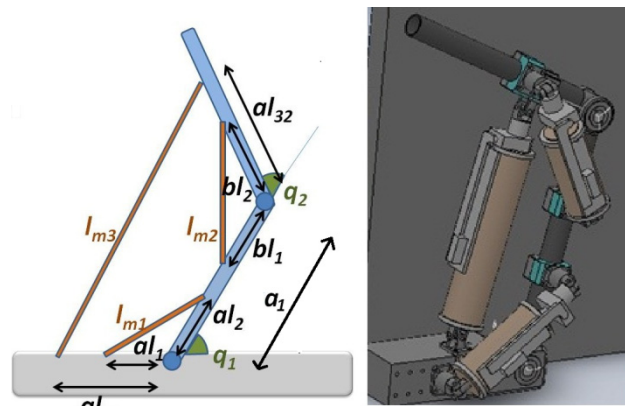

Figure 1. Simplified diagram and manipulator design

The main angles are the shoulder angle (q_1) and elbow angle (q_2). Based on the simplified diagram in Figure 1 and using trigonometric identities, the relationship of muscle lengths, l_{mi} with joint angles q_1 and q_2 is derived (a_1 and a_2 are link lengths).

$$l_{m1} = \sqrt{al_1^2 + al_2^2 + 2al_1 al_2 \cos q_1}$$

$$l_{m2} = \sqrt{bl_1^2 + bl_2^2 + 2bl_1 bl_2 \cos q_2}$$

$$l_{m3} = \sqrt{\begin{array}{l} al_{31}^2 + al_{32}^2 + a_1^2 + 2al_{31}a_1 \cos q_1 + \\ 2al_{32}a_1 \cos q_2 + 2al_{31}al_{32} \cos(q_1 + q_2) \end{array}} \quad (1)$$

Distances between connection lengths of the monoarticulars from the joint angles are labelled al_1, al_2, bl_1 and bl_2 while connection lengths of biarticular are al_{31} and al_{32}. The extension/contraction of monoarticular muscles affect the respective joint angles to which they attach, i.e., l_{m1} affects the joint angle q_1 (shoulder) and l_{m1} affects q_2 (elbow). However, the biarticular muscle l_{m3} is redundant because it affects both q_1 and q_2.

Based on (1), the relation between muscle velocities, $\dot{l}_m$ and joint velocities, $\dot{q}$ is given as;

$$\begin{bmatrix} \dot{l}_{m1} \\ \dot{l}_{m2} \\ \dot{l}_{m3} \end{bmatrix} = J_{lmq} \begin{bmatrix} \dot{q}_1 \\ \dot{q}_2 \end{bmatrix} \quad (2)$$

Where J_{lmq} is the muscle-to-joint space Jacobian, obtained from partial derivatives of (1) with respect to shoulder and elbow angles, shown in (3).

$$J_{lmq} = \begin{bmatrix} \dfrac{\partial l_{m1}}{\partial q_1} & \dfrac{\partial l_{m1}}{\partial q_2} \\ \dfrac{\partial l_{m2}}{\partial q_1} & \dfrac{\partial l_{m2}}{\partial q_2} \\ \dfrac{\partial l_{m3}}{\partial q_1} & \dfrac{\partial l_{m3}}{\partial q_2} \end{bmatrix} \quad (3)$$

where

$$\frac{\partial l_{m1}}{\partial q_1} = -\frac{al_1 al_2 sin(q_1)}{l_{m1}} \; ; \qquad \frac{\partial l_{m1}}{\partial q_2} = 0;$$

$$\frac{\partial l_{m2}}{\partial q_1} = 0; \qquad \frac{\partial l_{m2}}{\partial q_2} = -\frac{bl_1 bl_2 sin(q_2)}{l_{m2}};$$

$$\frac{\partial l_{m3}}{\partial q_1} = \frac{-al_{31}a_1 sin(q_1) - al_{31}al_{32} sin(q_1 + q_2)}{l_{m3}};$$

$$\frac{\partial l_{m3}}{\partial q_2} = \frac{-al_{32}a_1 sin(q_2) - al_{31}al_{32} sin(q_1 + q_2)}{l_{m3}}$$

It needs to be highlighted that this Jacobian is different from that of [6], because in the mentioned reference it is not structure-dependent. In our case, this Jacobian varies with the connection points (i.e., $al_1, al_2, bl_1, bl_2, al_{31}$ and al_{32}). Next, the equation relating joint torques, $\boldsymbol{\tau}$ (vector of shoulder and elbow torques) and muscle forces, $\boldsymbol{F_{lm}}$ (vector of muscle 1, muscle 2 and muscle 3 forces) can be described in (4) as;

$$\begin{bmatrix} \tau_1 \\ \tau_2 \end{bmatrix} = J_{lmq}^{\;\;T} \begin{bmatrix} F_{lm1} \\ F_{lm2} \\ F_{lm3} \end{bmatrix} \qquad (4)$$

Also, the equation relating the joint torques, $\boldsymbol{\tau}$ and the end-effector forces, $\boldsymbol{F_e}$ for a 2R planar manipulator is;

$$\begin{bmatrix} \tau_1 \\ \tau_2 \end{bmatrix} = J^T \begin{bmatrix} F_{ex} \\ F_{ey} \end{bmatrix} \qquad (5)$$

where J is the 2R planar Jacobian matrix from task space to joint space which contains the following elements;

$$\begin{bmatrix} -a_1 sin(q_1) - a_2 sin(q_1 + q_2) & -a_2 sin(q_1 + q_2) \\ a_1 cos(q_1) + a_2 cos(q_1 + q_2) & a_2 cos(q_1 + q_2) \end{bmatrix}$$
$$(6)$$

The equation relating to the end-effector forces, $\boldsymbol{F_e}$ (vector of end-effector forces) and the muscle forces, $\boldsymbol{F_{lm}}$ can be determined as follows;

$$\begin{bmatrix} F_{ex} \\ F_{ey} \end{bmatrix} = J^{T-1} J_{lmq}^{\;\;T} \begin{bmatrix} F_{lm1} \\ F_{lm2} \\ F_{lm3} \end{bmatrix} \qquad (7)$$

From Equation (6), the end-effector forces plot of the biarticular structure can be obtained. Figure 2 shows the static end-effector forces of structures with biarticular forces and the structures without. The forces applied for l_{m1} [N], l_{m2} [N] and l_{m3} [N] are;

$$\begin{aligned} -100\,[N] &\leq F_{lm1} \leq 100\,[N] \\ -100\,[N] &\leq F_{lm2} \leq 100\,[N] \\ -100\,[N] &\leq F_{lm3} \leq 100\,[N] \end{aligned} \qquad (8)$$

The end-effector output force produced by biarticular forces shows a hexagonal shape which is more homogenous than the tetragonal shape of the end-effector forces without biarticular actuation. This is one of the many advantages of biarticular manipulators compared to monoarticular actuation only.
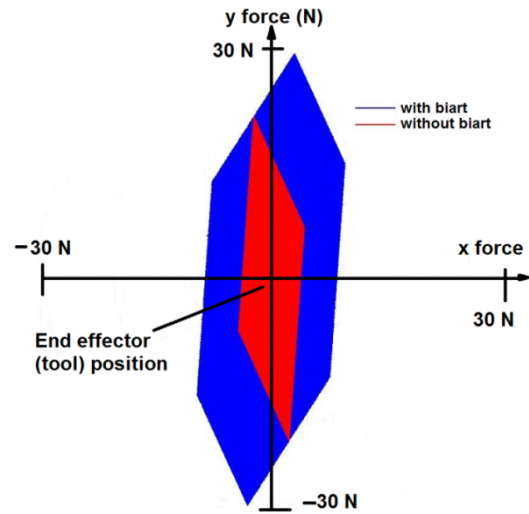

Figure 2. Cartesian view of end-effector forces for structures with (red) and without (blue) biarticular muscle forces

3. The Spiral Motor

Being specifically developed for musculoskeletal robotics, the third prototype spiral motor's main feature is its direct drive high thrust force actuator with high backdrivability. This three phase permanent magnet motor consists of a helical structure mover with permanent magnet and stator. The linear motion is derived from the spiral motion of the mover to drive the load. In addition, the motor has high thrust force characteristics because the flux is effectively utilized in its three dimensional structure [14]. This spiral motor does not include ball screw mechanisms, thus friction is negligible under proper air gap (magnetic levitation) control.
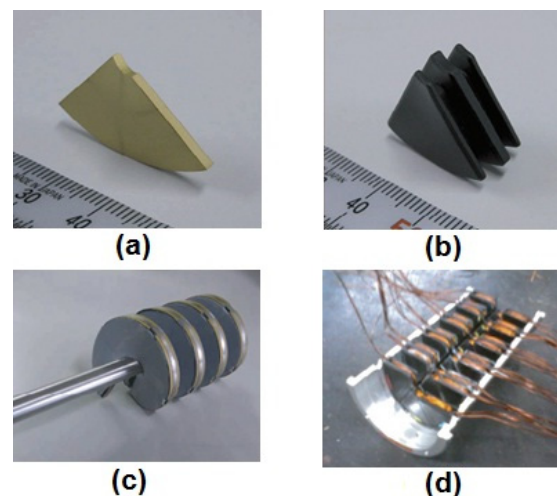

Figure 3. Spiral motor parts (a) Neodymium magnet (b) Silicon steel stator yoke (c) Mover attached with magnet and Teflon sheet (d) Wound and assembled half stator
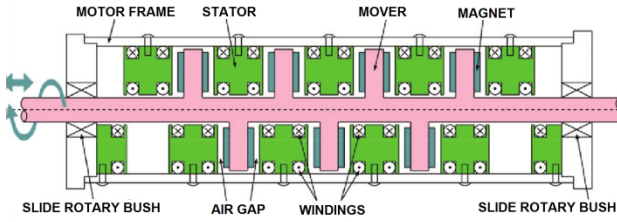
Figure 4. Spiral motor illustration

As seen in Figure 4, there is a small air gap between the mover and stator. This small distance is ideally 700 um between the Teflon sheet of the mover (at centre position) and the stator yoke. This air gap displacement, x_g, is related to the linear displacement, x, and angular displacement, θ, in (11). If the gap displacement is maintained, i.e., the surface of mover and stator are untouched, magnetic levitation is realized. Simultaneously, by a vector control strategy, the angular control provided by q-axis currents will give forward or backward thrust while d-axis currents control linear displacements and magnetic levitation, as shown in the plant dynamics of the spiral motor in (9) to (12);

$$M_s \ddot{x} = K_f I_d + K_g x_g - d_{xs} \tag{9}$$
$$J_s \ddot{\theta} = K_\tau I_q - h(K_f I_d + K_g x_g) - d_\theta \tag{10}$$
$$x_g = x - h\theta \tag{11}$$
$$h = \frac{l_p}{2\pi} \tag{12}$$

where $M_s \ddot{x}$ and $J_s \ddot{\theta}$ denote spiral motor force and torque, $K_g x_g$ represents the force generated during magnetic levitation, K_f is force constant and K_τ is torque constant. d_{xs} and d_θ are force and angular disturbances. Gap displacements, x_g, are related to linear, x, and angular displacements, θ, by the lead length, l_p (12). One revolution of θ would result in a displacement of length l_p if the gap displacement is zero.
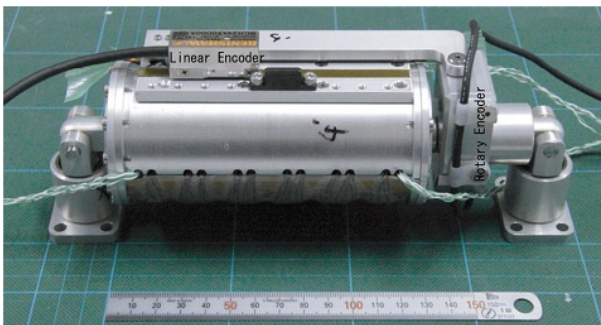

Figure 5. Assembled short-length spiral motor

3.1 Direct Drive Control of the Spiral Motor

Assume u_{xg} and u_θ are control inputs for gap displacement and angular displacement [15], which will match its respective acceleration terms;

$$u_{xg} = K_{pg}\left(x_{g0} - x_g\right) + K_{dg}\left(\dot{x}_{g0} - \dot{x}_g\right) \tag{13}$$
$$u_\theta = \ddot{\theta}_{ref} + K_{pt}\left(\theta_{ref} - \theta\right) + K_{dt}\left(\dot{\theta}_{ref} - \dot{\theta}\right) \tag{14}$$

where x_{g0} is the gap reference and $\dot{x}_{g0}$ is the gap velocity reference. K_{pg}, K_{dg}, K_{pt} and K_{dt} are PD gains for gap and angular positions and velocities. Also, the relation between linear and angular acceleration is known as;

$$\ddot{x} = \ddot{x}_g + h\ddot{\theta} \tag{15}$$

By replacing the linear acceleration term in (9) with (15), force dynamics of (9) can also be expressed as;

$$M\left(\ddot{x}_g + h\ddot{\theta}\right) = K_f I_d + K_g x_g - d_{xs} \tag{16}$$

Replacing the acceleration terms with control inputs (subscript n denotes nominal value);

$$M_n\left(u_{xg} + hu_\theta\right) = K_{fn}I_{dref} + K_{gn}x_g - \hat{d}_{xs} \tag{17}$$

Thus, the d-axis current reference (that will be tracked by a PI current controller) will have the following form;

$$I_{dref} = \frac{1}{K_{fn}}\left(M_n\left(u_{xg} + hu_\theta\right) - K_{gn}x_g + \hat{d}_{xs}\right) \tag{18}$$

By applying the same technique to the torque dynamics in (9) for the q-axis current reference;

$$J_n u_\theta = K_\tau I_{qref} - h\left(M_n\left(u_{xg} + hu_\theta\right) + \hat{d}_{xs}\right) + \hat{d}_\theta \tag{19}$$
$$I_{qref} = \frac{1}{K_\tau}\left(J_n u_\theta + h\left(M_n\left(u_{xg} + hu_\theta\right) + \hat{d}_{xs}\right) + \hat{d}_\theta\right) \tag{20}$$

and disturbance for linear displacement and angular displacement (in Laplace domain) are estimated as;

$$\hat{d}_{xs} = \frac{g_x}{s+g_x}\left(K_f I_{dref} + K_g x_g - sM_n\dot{x}\right) \tag{21}$$
$$\hat{d}_\theta = \frac{g_\theta}{s+g_\theta}\left(K_\tau I_{qref} - h\left(K_f I_{dref} + K_g x_g\right) - sJ_n\dot{\theta}\right) \tag{22}$$

where g_x and g_θ are the gain of the disturbance observer for linear and angular displacements. Until this point, direct drive control can be achieved at gap values of 0 mm. But due to disturbances (i.e., manufacturing accuracy of mover and stator), the current at 0 mm is not zero. Therefore, a neutral point (zero power) that induces zero currents for d-axis current is desired and low power control is realized as follows;
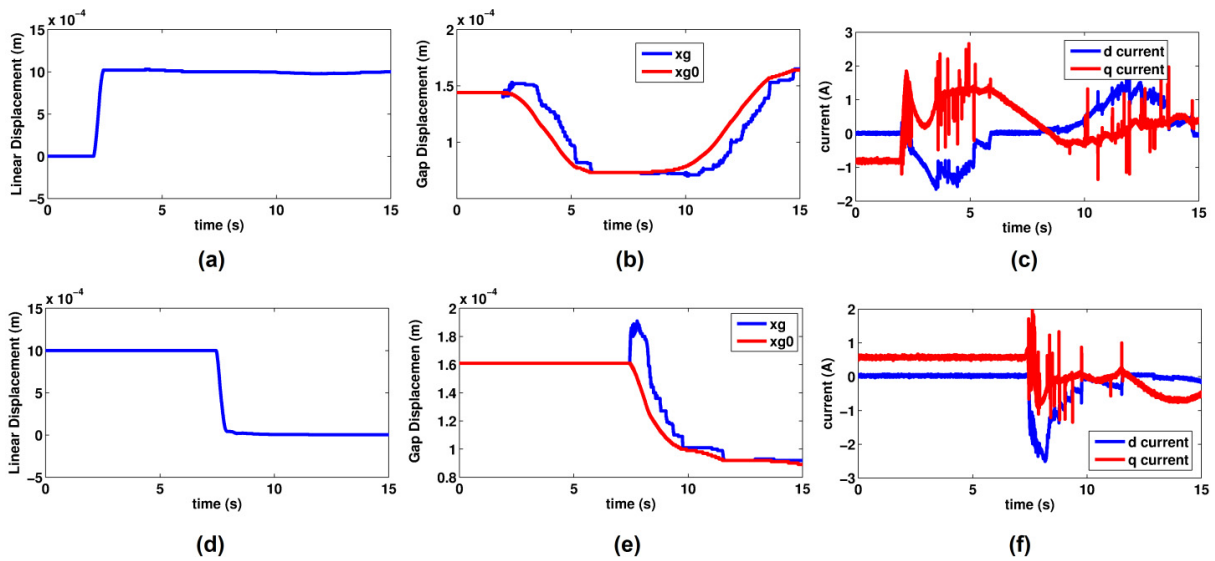
$$M_n\left(\ddot{x}_g + h\ddot{\theta}\right) = K_f\left(0\right) + K_g x_g - \hat{d}_{xs} \tag{23}$$
$$M_n\left(\ddot{x}_{g0} + h\ddot{\theta}\right) = 0 + K_g\left(x_{g0}\right) - \hat{d}_{xs}$$
$$x_{g0} = \frac{M_n\left(\ddot{x}_{g0} + h\ddot{\theta}\right) + \hat{d}_{xs}}{K_g}$$

As acceleration terms are usually affected by noise (due to differentiation), for initial testing, we simplify (24) to become;

$$x_{g0} = \frac{\hat{d}_{xs}}{K_g} \tag{24}$$

Figure 6. Direct drive experimental results with zero d-axis current control (a) Forward drive (b) Gap displacements (red denotes zero d-axis gap reference) (c) Currents (d) Reverse drive (e) Gap displacement (f) Currents

Experiments for direct drive forward and reverse motion were carried out using the monoarticular spiral motor with a stroke of 0.06 m. TMS320C6713-225MHz were used for data collection and control. Two DC supplies for the forward and backward inverters were used. At first, the direct drive control was applied to 0 mm (x position). We regard this as the initial gap stabilization phase. This is required because once magnetic levitation is realized, then forward and backward motions can be performed smoothly. If magnetic levitation and forward/back motions are performed simultaneously, the gap might not be maintained and damage could be inflicted on the stator and mover. After d-axis current stabilized at around 0 A, the forward reference was given. Then after the current stabilize at 0 A again, the reverse reference of 0 mm was applied. Figure 6 shows the experimental results for direct drive forward/reverse motion with zero d-axis current control (after gap initialization). Note that in [15], direct drive control was performed without zero d-axis control.

4. Singularity/manipulability of Biarticular Structure

This kinematic parameters can be used to determine the work space of the manipulator. The parameters of the three spiral motors are shown in Table 1.

	Spiral Motor Type	
Parameters	Monoarticular	Biarticular
Weight (kg)	1.5	2.3
Stroke (mm)	60	70
Extended length (mm)	256.5	380.5
Contracted length (mm)	196.5	310.5
Estimated max. force [N]	100	150

Table 1. Spiral motor specifications for muscles

The forward kinematics (end-effector position) of a 2R manipulator can be calculated by using the following equation (x and y are Cartesian coordinates);

$$x = a_1 \cos(q_1) + a_2 \cos(q_1 + q_2) \quad (25)$$
$$y = a_1 \sin(q_1) + a_2 \sin(q_1 + q_2) \quad (26)$$

For the biarticular manipulator, kinematic limits are due to the maximum (α_2, β_2) and minimum length (α_1, β_1) of the actuators, shown as;
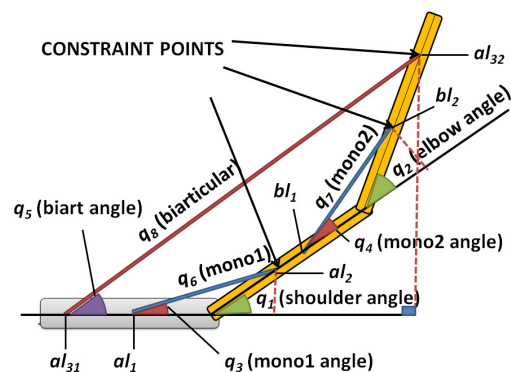
$$\alpha_1 \le l_{m1}, l_{m2} \le \alpha_2 \quad (27)$$
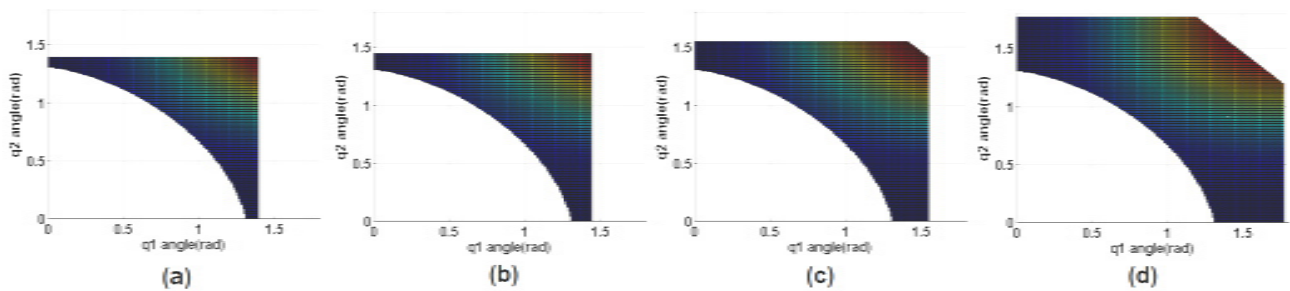$$\beta_1 \le l_{m3} \le \beta_2 \quad (28)$$

By referring to Equation (1), joint angle q_1 is bounded to the connection lengths al_1 and al_2. The same applies for monoarticular l_{m2}. For us, we chose $al_1 = bl_1$ and $al_2 = bl_2$ (same arrangement for both monoarticulars).

Then, the ranges of allowable angles for q_1 and q_2 are;

$$cos^{-1} \frac{(\alpha_2^2 - u)}{v} \le q_1, q_2 \le cos^{-1} \frac{(\alpha_1^2 - u)}{v} \quad (29)$$

Figure 7. Closed-kinematics of biarticular manipulator

www.intechopen.com

Ahmad Zaki bin Hj Shukor and Yasutaka Fujimoto:
Planar Task Space Control of a Biarticular Manipulator Driven by Spiral Motors
5

Figure 8. Manipulability plots for (a) al_1=0.14m, (b) al_1=0.16m, (c) al_1=0.18m and (d) al_1=0.20m for similar elbow monoarticular connection ($al_1 = bl_1$). Biarticular connections (al_{31} and al_{32}) set at 0.06 m
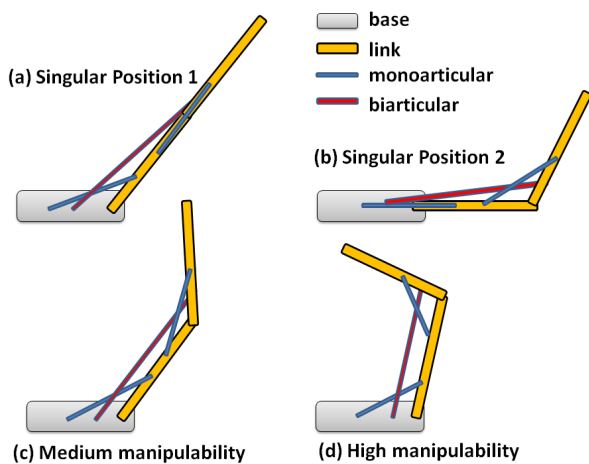
where

$$u = al_1^2 + al_2^2; \qquad v = 2al_1 al_2$$

This implies that the minimum lengths of monoarticulars incur maximum angles and vice versa. Thus, considering biarticular length limits, manipulability [16] can be plotted. Figure 8 shows the manipulability plots for different connecting points of monoarticular muscles. The shape of the angle limits is due to biarticular and monoarticular length limits. It can be seen that the further the connection points of monoarticulars are from the shoulder angle, the larger the work space.

Manipulability was obtained by finding the determinants of the muscle-joint Jacobian and end-effector-joint Jacobian terms. Dark blue represents low manipulability regions, and at zero manipulability, singularity is induced. Red represents the high manipulability region.

The inverse kinematic singularity of planar 2R manipulator [24] can be seen at the elbow angle of 0 radians. This is also true for the biarticular manipulator. In addition, due to muscle Jacobian terms, singularity is also evident at the shoulder angle of 0 radians. Some examples of singularity and manipulability poses for the biarticular manipulator are illustrated in Figure 9.
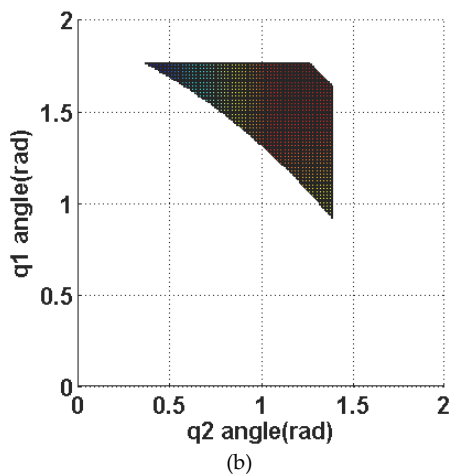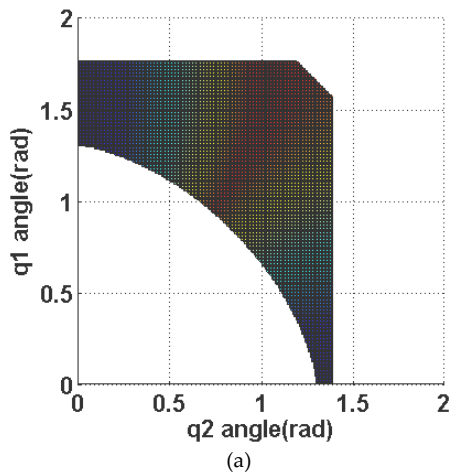
In the case that either shoulder or elbow monoarticular becomes fully extended, the shoulder/elbow angle becomes zero, and singularity is observed. However, both angles could not become zero simultaneously, due to biarticular length limit (refer Figure 7).

Higher manipulability poses are induced when lengths of muscles are short, and at near minimum lengths of muscles (or maximum angles), maximum manipulability region is observed.

If the connection points of shoulder and elbow monoarticulars are different, the following results of reciprocal condition of the Jacobian (another method to determine ill-condition [25]) is shown in Figure 10 and Figure 11;

(a)

(b)
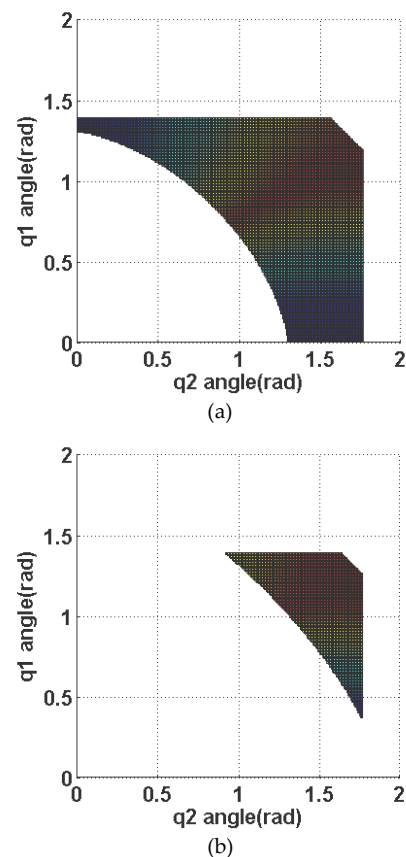
Figure 10. Reciprocal condition plot for $al_1 \neq bl_1$, $al_1 = 0.2$ m $bl_1 = 0.14$ m; (a) $al_{31} = al_{32} = 0.06$ m (b) $al_{31} = al_{32} = 0.10$ m

Figure 9. Examples of singular and manipulability poses for biarticular structure.

(a)

(b)

Figure 11. Reciprocal condition plot; $al_1 \neq bl_1$, $al_1 = 0.14$ m and $bl_1 = 0.2$ m; (a) $al_{31} = al_{32} = 0.06$ m (b) $al_{31} = al_{32} = 0.10$ m

As seen in Figure 10 and 11, if the value of al_1 or bl_1 is small, the corresponding shoulder/elbow angle becomes narrow and vice versa. Also, the further the biarticular muscle connection point is from the hinges, the smaller the work space becomes. By increasing the biarticular connection distance, ill-condition is further avoided, but with less work space.
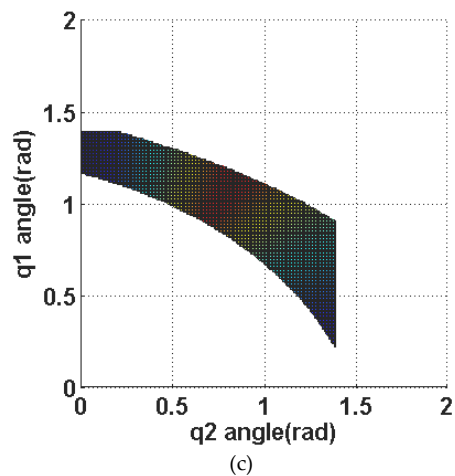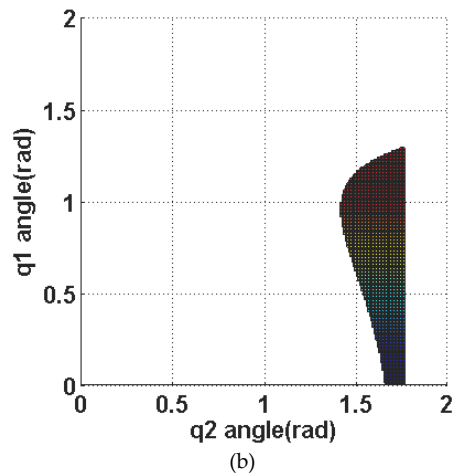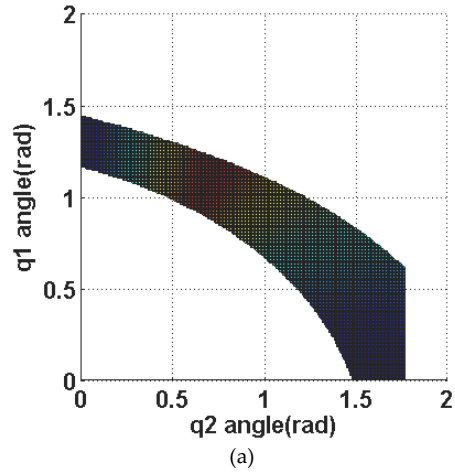
Figure 12 shows the reciprocal condition plot with different connection points of the biarticular muscle. It is obvious that by connecting the end of each side of the biarticular muscle differently, significant changes to the work space and reciprocal condition is seen.

5. Biarticular Plant Dynamics Modelling

Most planar 2R robots are serial/open-chain manipulators. There is much research on control of these 2R manipulators. Modelling of unconstrained open-chain manipulators uses Ordinary Differential Equations (via Lagrange (LE) or Newton Euler (NE) formulation), while closed-chain manipulators require Differential Algebraic Equations due to constraint equations [17]. Constraint

points are virtually cut open and LE formulation was used to obtain mass, gravity and centrifugal matrices. Equation (29) depicts the generalized equations of motion of a closed-chain manipulator;

$$M_c(q)\ddot{q} + C(q,\dot{q})\dot{q} + G(q) = \tau + J_c^T \lambda + J^T \, d_{xy} \qquad (29)$$

(a)

(b)

(c)

Figure 12. Reciprocal condition plot; $al_1 = bl_1 = 0.2$ m; (a) $al_{31} = 0.06$ m, $al_{32} = 0.10$ m (b) $al_{31} = 0.08$ m, $al_{32} = 0.06$ m; (c) $al_1 = bl_1 = 0.14$ m $al_{31} = 0.06$ m, $al_{32} = 0.10$ m

www.intechopen.com

Ahmad Zaki bin Hj Shukor and Yasutaka Fujimoto: 7
Planar Task Space Control of a Biarticular Manipulator Driven by Spiral Motors

where $\boldsymbol{q}$ denotes joint angle/muscle length vector, $\boldsymbol{\lambda}$ is the vector of constraints, $M_c(q)$ is the mass matrix, $C(q, \dot{q})$ are centrifugal/Coriolis terms, $G(q)$ are gravity terms, $\boldsymbol{\tau}$ are generalized forces/torques, $J_c^T \lambda$ are the constraint forces (from the closed-loop kinematics). The term $J^T \boldsymbol{d}_{xy}$ represents disturbance forces applied. J^T is transposed from (6) and $\boldsymbol{d}_{xy}$ is a vector of x and y Cartesian disturbance force. We will show the constraint-related terms. As mentioned, others can be obtained via LE, NE or other dynamics formulation.

Constraint equations (from trigonometry) are derived as;

$$
\begin{aligned}
q_6 \cos(q_3) - al_1 - al_2 \cos(q_1) &= 0 \\
q_6 \sin(q_3) - al_2 \sin(q_1) &= 0 \\
q_7 \cos(q_4) - bl_1 - bl_2 \cos(q_2) &= 0 \\
q_7 \sin(q_4) - bl_2 \sin(q_2) &= 0 \\
q_8 \cos(q_5) - al_{31} - a_1 \cos(q_1) - al_{32}\cos(q_1 + q_2) &= 0 \\
q_8 \sin(q_5) - a_1 \sin(q_1) - al_{32} \sin(q_1 + q_2) &= 0
\end{aligned}
$$

Also, the relative acceleration at the constraints are zero ($J_c, \dot{J_c}$ are the constraint Jacobian and Jacobian derivative),

$$J_c \ddot{\boldsymbol{q}} + \dot{J_c} \dot{\boldsymbol{q}} = 0 \qquad (30)$$

The constraint Jacobian (unmentioned terms are zero) is described as;

$$J_c = \begin{bmatrix} J_{c11} & \cdots & J_{c18} \\ \vdots & \ddots & \vdots \\ J_{c61} & \cdots & J_{c68} \end{bmatrix} \qquad (31)$$

$$
\begin{array}{ll}
J_{c11} = al_2 \sin(q_1); & J_{c13} = -q_6 \sin(q_3); \\
J_{c16} = \cos(q_3); & J_{c21} = -al_2 \cos(q_1); \\
J_{c23} = q_6 \cos(q_3); & J_{c26} = \sin(q_3); \\
J_{c32} = bl_2 \sin(q_2); & J_{c34} = -q_7 \sin(q_4); \\
J_{c37} = \cos(q_4); & J_{c42} = -bl_2 \cos(q_2); \\
J_{c44} = q_7 \cos(q_4); & J_{c47} = \sin(q_4); \\
\end{array}
$$
$$
\begin{aligned}
J_{c51} &= al_{32} \sin(q_1 + q_2) + a_1 \sin(q_1); \\
J_{c52} &= al_{32} \sin(q_1 + q_2); \\
\end{aligned}
$$
$$
\begin{array}{ll}
J_{c55} = -q_8 \sin(q_5); & J_{c58} = \cos(q_5); \\
\end{array}
$$
$$
\begin{aligned}
J_{c61} &= -al_{32} \cos(q_1 + q_2) - a_1 \cos(q_1); \\
J_{c62} &= -al_{32} \cos(q_1 + q_2); \\
\end{aligned}
$$
$$
\begin{array}{ll}
J_{c65} = q_8 \cos(q_5); & J_{c68} = \sin(q_5); \\
\end{array}
$$

The constraint Jacobian derivative is derived as;

$$\dot{J_c} = \begin{bmatrix} J_{d11} & \cdots & J_{d18} \\ \vdots & \ddots & \vdots \\ J_{d61} & \cdots & J_{d68} \end{bmatrix} \qquad (32)$$

$$
\begin{aligned}
J_{d11} &= al_2 \cos(q_1)\dot{q}_1 \\
J_{d13} &= -q_6 \cos(q_3)\dot{q}_3 - \sin(q_3)\dot{q}_6; \\
J_{d16} &= -\sin(q_3)\dot{q}_3; \quad J_{d21} = al_2 \sin(q_1)\dot{q}_1; \\
J_{d23} &= -q_6 \sin(q_3)\dot{q}_3 + \cos(q_3)\dot{q}_6; \\
J_{d26} &= \cos(q_3)\dot{q}_3; \quad J_{d32} = bl_2 \cos(q_2)\dot{q}_2; \\
J_{d34} &= -q_7 \cos(q_4)\dot{q}_4 - \sin(q_4)\dot{q}_7; \\
J_{d37} &= -\sin(q_4)\dot{q}_4; \quad J_{d42} = bl_2 \sin(q_2)\dot{q}_2; \\
J_{d44} &= -q_7 \sin(q_4)\dot{q}_4 - \cos(q_4)\dot{q}_7; \\
J_{d47} &= \cos(q_4)\dot{q}_4; \\
J_{d51} &= a_1 \cos(q_1)\dot{q}_1 + al_{32}(\dot{q}_1 + \dot{q}_2)\cos(q_1 + q_2);
\end{aligned}
$$

$$
\begin{aligned}
J_{d52} &= al_{32}(\dot{q}_1 + \dot{q}_2)\cos(q_1 + q_2); \\
J_{d55} &= -q_8 \cos(q_5)\dot{q}_5 - \sin(q_5)\dot{q}_8; \\
J_{d58} &= -\sin(q_5)\dot{q}_5; \\
J_{d61} &= a_1 \sin(q_1)\dot{q}_1 + al_{32}(\dot{q}_1 + \dot{q}_2)\sin(q_1 + q_2); \\
J_{d62} &= al_{32}(\dot{q}_1 + \dot{q}_2)\sin(q_1 + q_2); \\
J_{d65} &= -q_8 \sin(q_5)\dot{q}_5 - \cos(q_5)\dot{q}_8; \\
J_{d68} &= \cos(q_5)\dot{q}_5;
\end{aligned}
$$

By combining these two equations, the following generalized closed-chain model can be derived;

$$\begin{bmatrix} M_c & -J_c^T \\ -J_c & 0 \end{bmatrix} \begin{bmatrix} \ddot{\boldsymbol{q}} \\ \boldsymbol{\lambda} \end{bmatrix} = \begin{bmatrix} \boldsymbol{\tau} - C\dot{\boldsymbol{q}} + J^T \boldsymbol{d}_{xy} \\ \dot{J_c} \dot{\boldsymbol{q}} \end{bmatrix} \qquad (33)$$

To include the spiral motor plant dynamics in the generalized closed-chain model, (33) has to be modified to the following;

$$\begin{bmatrix} M_c & 0 & -J_c^T \\ 0 & J_s & 0 \\ -J_c & 0 & 0 \end{bmatrix} \begin{bmatrix} \ddot{\boldsymbol{q}} \\ \ddot{\boldsymbol{\theta}} \\ \boldsymbol{\lambda} \end{bmatrix} = \begin{bmatrix} \boldsymbol{\tau} - C\dot{\boldsymbol{q}} + J^T \boldsymbol{d}_{xy} \\ \boldsymbol{\tau}_\theta \\ \dot{J_c} \dot{\boldsymbol{q}} \end{bmatrix} \qquad (34)$$

The inertia terms from the angular rotation now emerge ($J_s, \ddot{\theta}, \tau_\theta$). With this modification, the d and q-axis currents could also be seen in simulation (refer Equations (9) to (12)). To visualize the plant model, the dimensions of the left-hand terms would become;

$$
\begin{bmatrix}
M_{c11} & \cdots & M_{c18} & 0 & 0 & 0 & -J_{c11} & \cdots & -J_{c61} \\
\vdots & \ddots & \vdots & \vdots & \vdots & \vdots & \vdots & \ddots & \vdots \\
M_{c81} & \cdots & M_{c88} & 0 & 0 & 0 & -J_{c18} & \cdots & -J_{c68} \\
0 & \cdots & 0 & J_1 & 0 & 0 & 0 & \cdots & 0 \\
0 & \cdots & 0 & 0 & J_2 & 0 & 0 & \cdots & 0 \\
0 & \cdots & 0 & 0 & 0 & J_3 & 0 & \cdots & 0 \\
-J_{c11} & \cdots & -J_{c18} & 0 & 0 & 0 & 0 & \cdots & 0 \\
\vdots & \ddots & \vdots & \vdots & \vdots & \vdots & \vdots & \ddots & \vdots \\
-J_{c61} & \cdots & -J_{c68} & 0 & 0 & 0 & 0 & \cdots & 0
\end{bmatrix}
\begin{bmatrix}
\ddot{q}_1 \\ \vdots \\ \ddot{q}_8 \\ \ddot{\theta}_1 \\ \ddot{\theta}_2 \\ \ddot{\theta}_3 \\ \lambda_1 \\ \vdots \\ \lambda_6
\end{bmatrix}
$$
$$(35)$$

The linear acceleration of the spiral motors (i.e., $\ddot{x}_1, \ddot{x}_2, \ddot{x}_3$) are equivalent to $\ddot{q}_6, \ddot{q}_7, \ddot{q}_8$ and rotational acceleration of the motors are $\ddot{\theta}_1, \ddot{\theta}_2, \ddot{\theta}_3$. After integrating twice, a gap can then be obtained via (11). J_i are spiral motor inertias.

The right-hand terms of (34) would become;

$$
\begin{bmatrix}
\begin{bmatrix} \tau_1 \\ \vdots \\ \tau_8 \end{bmatrix} - \begin{bmatrix} C_{11} & \cdots & C_{18} \\ \vdots & \ddots & \vdots \\ C_{81} & \cdots & C_{88} \end{bmatrix} \begin{bmatrix} \dot{q}_1 \\ \vdots \\ \dot{q}_8 \end{bmatrix} + \begin{bmatrix} J_{11} & J_{21} & 0 & \cdots & 0 \\ J_{12} & J_{22} & 0 & \cdots & 0 \\ 0 & 0 & 0 & \cdots & 0 \\ \vdots & \vdots & \vdots & \cdots & 0 \\ 0 & 0 & 0 & \cdots & 0 \end{bmatrix} \begin{bmatrix} d_x \\ d_y \\ 0 \\ \vdots \\ 0 \end{bmatrix} \\
K_{\tau 1}I_{q1} - h_1(K_{f1}I_{d1} + K_{g1}x_{g1}) \\
K_{\tau 2}I_{q2} - h_2(K_{f2}I_{d2} + K_{g2}x_{g2}) \\
K_{\tau 3}I_{q3} - h_3(K_{f3}I_{d3} + K_{g1}x_{g3}) \\
\begin{bmatrix} J_{d11} & \cdots & J_{d18} \\ \vdots & \ddots & \vdots \\ J_{d61} & \cdots & J_{d68} \end{bmatrix} \begin{bmatrix} \dot{q}_1 \\ \vdots \\ \dot{q}_8 \end{bmatrix}
\end{bmatrix}
$$
$$(36)$$

The unactuated variables are q_1 to q_5. Thus, its corresponding τ_1 to τ_5 are always 0 (no input torque/force). τ_θ is the vector of spiral motor torques. τ_6 to τ_8 (monoarticular 1, monoarticular 2 and biarticular forces) are given by the following equation;

$$\begin{bmatrix} \tau_6 \\ \tau_7 \\ \tau_8 \end{bmatrix} = \begin{bmatrix} K_{f1}I_{d1} + K_{g1}x_{g1} \\ K_{f2}I_{d2} + K_{g2}x_{g2} \\ K_{f3}I_{d3} + K_{g1}x_{g3} \end{bmatrix} \qquad (37)$$

In simplified terms, the plant can be described by (38);

$$\begin{bmatrix} \ddot{q} \\ \ddot{\theta} \\ \lambda \end{bmatrix} = \begin{bmatrix} M_c & 0 & -J_c^T \\ 0 & J_s & 0 \\ -J_c & 0 & 0 \end{bmatrix}^{-1} \begin{bmatrix} \tau - C\dot{q} + J^T \, d_{xy} \\ \tau_\theta \\ \dot{J}_c\dot{q} \end{bmatrix} \qquad (38)$$

6. Work Space Position Control

Robotic manipulators have been researched extensively; some of the many examples are torque sensorless control [18], SCARA manipulator tracking control [19], feedforward and computed torque control [20] and position control of constrained robotic system [21]. Previously described in [22] are some approaches (the IK approach and the Direct Cartesian (DC) approach) for the general structure of a biarticular manipulator, i.e., not actuator specific. In [23] other methods were investigated.

In this paper, the generalized work space control [22] is extended to the specific spiral motor case for the purpose of viewing the effects on gap and position control with the addition of Cartesian load disturbance. By considering a circular task space trajectory, the references for x and y-axis positions are shown as;

$$x(t) = A\cos(\omega(t)) + x_0 \qquad (39)$$
$$y(t) = A\sin(\omega(t)) + y_0 \qquad (40)$$
$$\omega(t) = 2\pi(1 - \cos(t)) \qquad (41)$$

where A is the radius of the circle and x_0 and y_0 are x and y coordinates of the centre of the circle.

From 0 to 0.5 seconds, gap stabilization is performed without giving any position reference (either in joint space or work space). This phase is to allow the gap to stabilize at centre (0mm) position. From 0.5 to 6 seconds, the position reference of the circle trajectory (5 cm radius) is given. In addition, Cartesian disturbance on the end-effector is given between 1 to 3 seconds.

Here we present comparisons of a monoarticular only actuated structure with that of a biarticular structure by using the IK approach and the DC approach (monoarticular control gains, i.e., PD, disturbance observer cut-off frequencies are identical). Note that for work space control, zero d-axis current control is not applied.

5.1 Inverse Kinematics Approach

By using the IK approach [24], joint space trajectories (elbow/shoulder angles) are obtained from the Cartesian reference trajectories (x and y);

$$D = \frac{x^2 + y^2 - a_1^2 - a_2^2}{2a_1 a_2} \qquad (42)$$

$$q_2 = \tan^{-1}\sqrt{\frac{1 - D^2}{D}} \qquad (43)$$

$$q_1 = \tan^{-1}\frac{y}{x} - \tan^{-1}\left(\frac{a_2\sin(q_2)}{a_1 + a_2\cos(q_2)}\right) \qquad (44)$$

From joint references, muscle kinematics (1) can be used to obtain muscle references (i.e., length, velocity, acceleration). $\ddot{x}_1, \ddot{x}_2, \ddot{x}_3$ are shoulder, elbow monoarticular and biarticular spiral motor linear accelerations.

$$\ddot{q}_{6ref} = \ddot{l}_{m1_{ref}} = \ddot{x}_{1ref} \qquad (45)$$
$$\ddot{q}_{7ref} = \ddot{l}_{m2_{ref}} = \ddot{x}_{2ref} \qquad (46)$$
$$\ddot{q}_{8ref} = \ddot{l}_{m3_{ref}} = \ddot{x}_{3ref} \qquad (47)$$

The rotational acceleration references are calculated as in (48) to (50) with $\ddot{x}_{gi_0} = 0$ (gap references are zero for non-zero d-axis current control);

$$\ddot{\theta}_{1ref} = \frac{\ddot{x}_{g1_0} - \ddot{q}_{6ref}}{h_1} \qquad (48)$$

$$\ddot{\theta}_{2ref} = \frac{\ddot{x}_{g2_0} - \ddot{q}_{7ref}}{h_2} \qquad (49)$$

$$\ddot{\theta}_{3ref} = \frac{\ddot{x}_{g3_0} - \ddot{q}_{8ref}}{h_3} \qquad (50)$$

From these references, dq-axis control (refer (13) to (20)) can be constructed for each muscle to generate the forces ($\tau_6, \tau_7 \, \tau_8$) and torques ($\tau_{\theta1}, \tau_{\theta2,}\tau_{\theta3}$) as in (36) and (37).
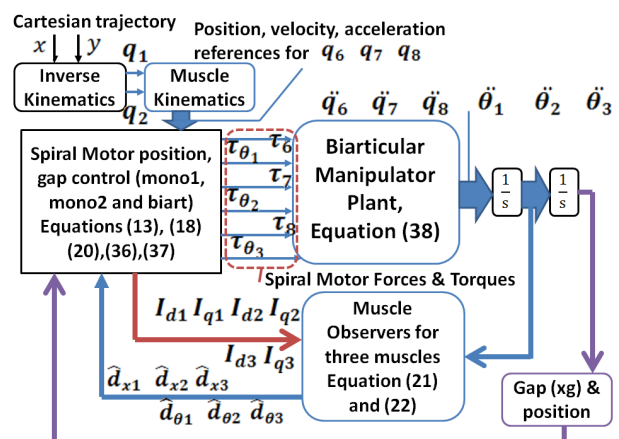

Figure 13. IK control for manipulator driven by spiral motors

www.intechopen.com

Ahmad Zaki bin Hj Shukor and Yasutaka Fujimoto: 9
Planar Task Space Control of a Biarticular Manipulator Driven by Spiral Motors

In this part, only Y-axis disturbance of 10 [N] is given. The initial circle trajectory response in Figure 14 shows that the biarticular structure exhibits better accuracy. Initial errors due to the gap stabilization can be seen at the near start position (0.15, 0.53). Then the effect disturbance of 10 [N] can be seen as the response is deviating from the reference. Cartesian errors are shown in Figure 15; 'mono' denotes monoarticular structure responses while 'biart' denotes biarticular structure responses.
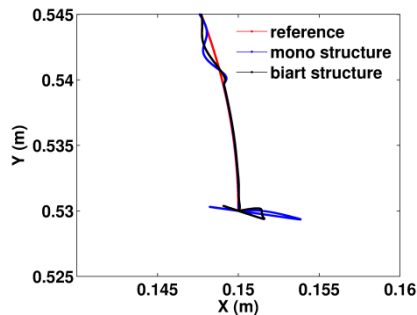
Figure 14. Close-up view of circle trajectory responses from monoarticular structure and biarticular structure
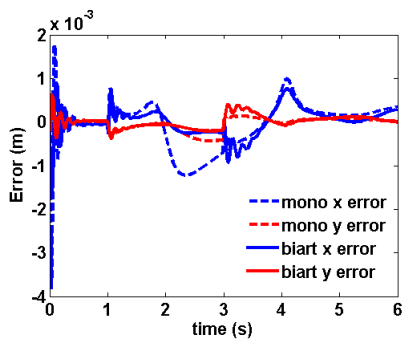
Figure 15. Cartesian errors for the IK approach
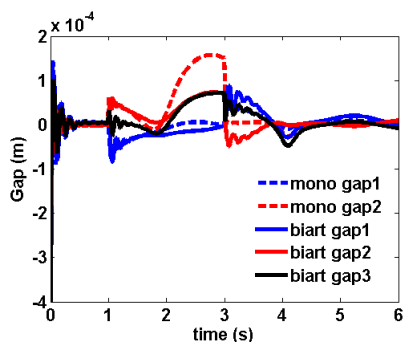
Figure 16. Gap responses for the IK approach

For Figure 16, 'mono gap1' and 'mono gap2' refer to the monoarticular muscle gaps in the monoarticular structure, while 'biart gap1', 'biart gap2', 'biart gap3' refer to the shoulder monoarticular gap, elbow monoarticular gap and biarticular gap in the biarticular structure. Referring to gap displacement responses in Figure 16, in the initial gap stabilization phase (0 to 0.5 s), more interaction is obvious in the biarticular case, but the biarticular structure shows better gap control during position tracking.

Force responses from muscles are shown in Figure 17. Both forces are bounded. Next, the torque responses (rotational part of spiral motor) are shown in Figure 18.
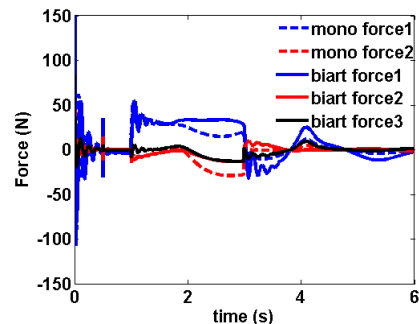

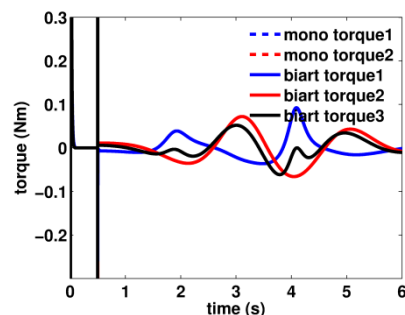**Figure 17.** Spiral motor forces for the IK approach

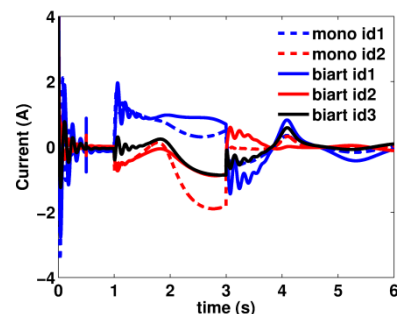**Figure 18.** Spiral motor torque for the IK approach

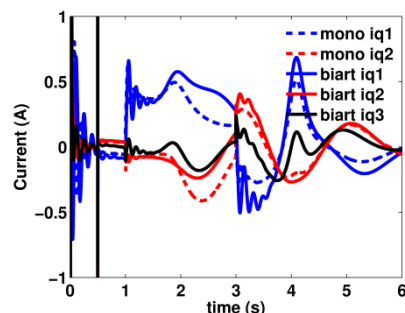**Figure 19.** D-axis current for the IK approach

Figure 20. Q-axis current for the IK approach

Figures 19 and 20 show the d- and q-axis currents generated. As in the spiral motor simplified plant model, the d-axis is related to muscle (spiral motor) forces while the q-axis is related to spiral motor torques. It can be said that the biarticular forces reduce the effort of the elbow monoarticular muscle, but increase shoulder muscle actuation.

For this approach, muscle force interactions are clearly visible (seen in oscillations) as expected, because the muscles are independently controlled without any force distribution.

5.2 Direct Cartesian Approach

For the DC approach, the forces from work space/task space domain are controlled in the shoulder and elbow joint space (virtually), then transferred to the actuator (muscle) space by the joint-muscle Jacobian (3).

Figure 21 shows the control diagram and the control equation is shown in Equation (51) to (55). x_{res}, y_{res} are Cartesian end-effector position responses.

$$\begin{bmatrix} \tau_1 \\ \tau_2 \end{bmatrix} = MJ^{-1} \left[\begin{bmatrix} \ddot{x} \\ \ddot{y} \end{bmatrix} - \dot{J} \begin{bmatrix} \dot{q}_1 \\ \dot{q}_2 \end{bmatrix} + \begin{bmatrix} K_{p_1} & 0 \\ 0 & K_{p_2} \end{bmatrix} \begin{bmatrix} x - x_{res} \\ y - y_{res} \end{bmatrix} + \begin{bmatrix} K_{d_1} & 0 \\ 0 & K_{d_2} \end{bmatrix} \begin{bmatrix} \dot{x} - \dot{x}_{res} \\ \dot{y} - \dot{y}_{res} \end{bmatrix} \right] + \begin{bmatrix} \hat{\tau}_1 \\ \hat{\tau}_2 \end{bmatrix} \quad (51)$$

$$\begin{bmatrix} \hat{\tau}_1 \\ \hat{\tau}_2 \end{bmatrix} = \begin{bmatrix} \frac{g_1}{s+g_1} & 0 \\ 0 & \frac{g_2}{s+g_2} \end{bmatrix} \begin{bmatrix} \tau_1 - s\, m_{11} \dot{q}_1 \\ \tau_2 - s\, m_{22} \dot{q}_2 \end{bmatrix} \quad (52)$$

$$\begin{bmatrix} F_{lm1} \\ F_{lm2} \\ F_{lm3} \end{bmatrix} = J_{lmq}^{T}{}^{-1} \begin{bmatrix} \tau_1 \\ \tau_2 \end{bmatrix} \quad (53)$$

where

$$M = \begin{bmatrix} m_{11} & m_{12} \\ m_{21} & m_{22} \end{bmatrix}$$
$$m_{11} = m_1 l_{c1}^2 + m_2(l_1^2 + l_{c1}^2 + 2l_1 l_{c1} \cos(q_2))$$
$$+2l_1 l_{c1} + I_1 + I_2)$$
$$m_{12} = m_{21} = m_2(l_{c2}^2 + l_1 l_{c1}^2 \cos(q_2) + I_2)$$
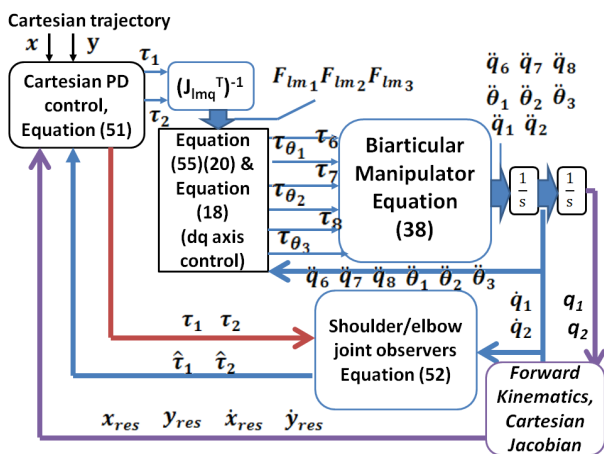$$m_{22} = m_2 l_{c2}^2 + I_2$$

Figure 21. DC control for manipulator

The inverse Jacobian to obtain the muscle forces, F_{lmi} are calculated by using Moore's inverse pseudomatrix. $\ddot{x}$ is Cartesian acceleration, J^{-1} is the inverse of (6), $\dot{J}$ is the Jacobian time derivative, M is 2R planar mass matrix and g_i are disturbance observer gains. Now that the muscle forces' terms are obtained from the virtual joint torques, it must be distributed to the gap and angular terms of the spiral motor. From Equation (16), the linear forces for the spiral motor is again shown;

$$M_s(\ddot{x}_g + h\ddot{\theta}) = M_s(u_{xg} + h u_\theta) = F_{lm_i} \quad (54)$$

The gap control variable (u_{xg}) is the same as in (13), but the angular control variable is obtained by manipulating Equation (54) (subscript i refers to respective muscle number);

$$u_{\theta_i} = \frac{\frac{F_{lm_i}}{M_{s_i}} - u_{xg_i}}{h_i} \quad (55)$$

For this study, Cartesian Y disturbance of 10 [N] is also added to the end-effector from the period of 1 to 3 seconds. The trajectory tracking and Cartesian errors are depicted in Figure 22 and Figure 23 which shows significant improvements compared to the IK approach.
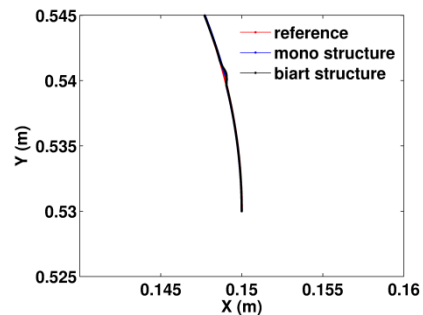

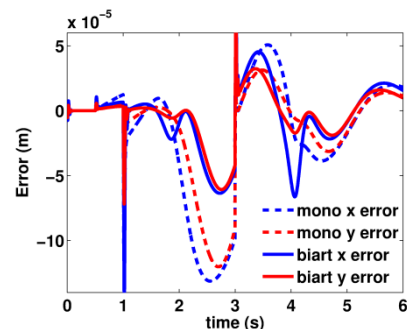**Figure 22.** Close-up view of circle trajectory responses for the DC approach

Figure 23. Cartesian errors for the DC approach

Next, the gap responses are shown in Figure 24. Biarticular muscle helps reduce gap values for monoarticulars, especially during disturbance.

The spiral motor force and torques are depicted in Figure 25 and Figure 26. Forces were acceptable and bounded between 60 [N] in both directions for all the muscles.
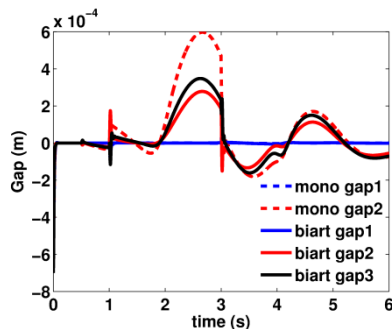

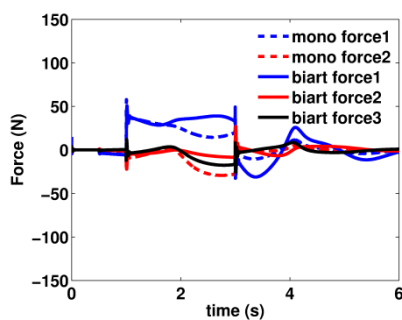**Figure 24.** Gap responses for the DC approach

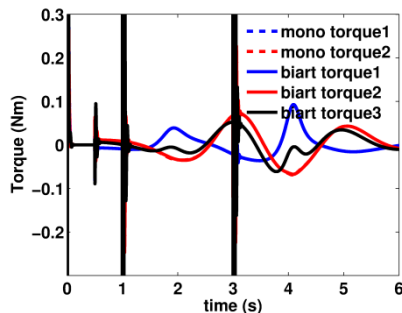**Figure 25.** Spiral motor forces for the DC approach

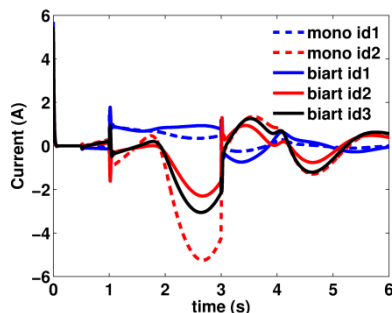**Figure 26.** Muscle torques for the DC approach

Figure 27. D-axis current for the DC approach

Next, spiral motor d- and q-axis currents are shown in Figure 27 and Figure 28. It can be seen that the d-axis current is lower in the biarticular structure than in the monoarticular only structure.
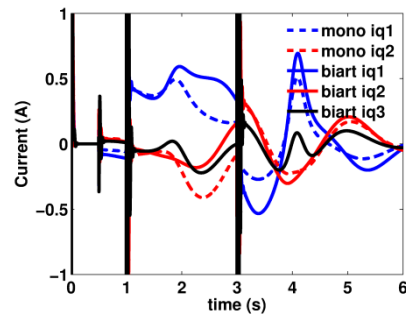

Figure 28. D-axis currents for the DC approach

7. Discussion

The two methods for position control in the task space/work space domain provide some interesting results. It is clear that the IK approach and the DC approach yield acceptable responses.

In the gap stabilization phase, IK provides a clear oscillatory response in achieving a gap at the centre (0 mm). The biarticular actuation increases the oscillations of the gaps. In the DC approach, this oscillation does not exist, in both monoarticular and biarticular structures. The DC approach provides smooth gap responses initially. At the start of position tracking (before disturbance), both methods yield good responses (i.e., variation of gap minimum, small amount of forces and currents), but during disturbance, the effects can be seen clearly. Tracking errors increase, but control was maintained. Towards the end of the disturbance, errors were acceptable.

Table 2 summarizes the comparisons of the IK and DC methods on monoarticular and biarticular structures based on Cartesian errors.

Error (mm)	Structure/Method			
	MonoIK	BiartIK	MonoDC	BiartDC
Mean x error	-0.070	-0.001	-0.017	-0.005
Mean y error	-0.039	0.007	-0.013	-0.003
Max. x error	3.800	1.600	0.131	0.149
Max. y error	0.651	0.617	0.120	0.085

Table 2. Comparison of errors between methods/structure

In short, errors for DC method are lower than IK method and errors for biarticular structures are lower than monoarticular structures.

8. Conclusion and Future Works

This paper has shown the proposed biarticular manipulator using spiral motors developed in our laboratory. The simplification and arrangements of the muscles and the end-effector-muscle-joint force

properties were initially presented. Then, the spiral motor was introduced and manipulability was discussed. Next, the modelling of the biarticular manipulator using spiral motors was briefly explained and the results of the IK approach and the DC approach for position control of the manipulator were compared between a monoarticular only structure and a biarticular structure. For work space force control schemes (with environment) of a biarticular manipulator, readers are advised to refer to [26].

The gap control is a crucial element in the spiral motor direct drive motion. It was shown that the work space position control was successful in all cases, although some better responses were shown in the biarticular manipulator. Among the advantages of the biarticular structure were the improved control of the gap of the elbow monoarticular muscle and better accuracy of trajectory tracking. In future, we plan to compare our manipulator to other biarticular manipulators available, i.e., ball-screw mechanism, pneumatics, cables or hydraulics.

9. Acknowledgments

10. References

[1] Park H. S, Floyd S, Sitti M (2010) Roll and Pitch Motion Analysis of a Biologically Inspired Quadruped Water Runner Robot. Int Journal of Robotic Research, Vol. 29, No. 10 : 1281-1297.

[2] Deng X, Schenato L, Wu W, Sastry S, (2006) Flapping Flight for Robotic Insects. I. System Modelling. IEEE Trans. on Robotics, Vol. 22, No. 4 : 776-788.

[3] Tahara K, Luo Z.W, Arimoto S, Kino H (2005) Task Space Feedback Control for a Two-link Arm Driven by Six Muscles with Variable Damping and Elastic Properties. IEEE Int. Conf. on Robotics and Automation : 223-228.

[4] Kino H, Kikuchi S, Yahiro T, Tahara K (2009) Basic Study of Biarticular Muscle's Effect on Muscular Internal Force Control Based on Physiological Hypotheses. IEEE Int. Conf. on Robotics and Automation : 4195-4220.

[5] Tahara K, Luo Z.W, Arimoto S, Kino H (2006) On Control Mechanisms of Human-Like Reaching Movements with Musculo-Skeletal Redundancy. IEEE Int. Conf. on Intelligent Robots and Systems : 1402-1409.

[6] Oh S, Hori Y (2009) Development of Two-Degree-of-Freedom Control for Robot Manipulator with Biarticular Muscle Torque. American Control Conference : 325-330.

[7] Tsuji T (2010) A Model of Antagonistic Triarticular Muscle Mechanism for Lancelet Robot. The 11th IEEE Int. Workshop on Advanced Motion Control : 496-501.

[8] Salvucci V, Kimura Y, Oh S, Hori Y (2011) BiWi: Bi-Articularly Actuated and Wire Driven Robot Arm. The IEEE Int. Conf. on Mechatronics : 827-832.

[9] Choi T.Y, Lee J.J (2010) Control of Manipulator using Pneumatic Muscles for Enhanced Safety. IEEE Trans. on Ind. Electronics, Vol. 57, no. 8 : 2815-2285.

[10] Hosoda K, Takayama H, Takuma T (2008) Bouncing Monopod with Bio-mimetic Musculor-Skeleton System. Int. Conf. on Intelligent Robots and Systems : 3083-3088.

[11] Niiyama R, Nagakubo A, Kuniyoshi Y (2007) Mowgli: A Bipedal Jumping and Landing Robot with an Artificial Musculoskeletal System. Int. Conf. on Robotics and Automation : 2546-2551.

[12] Reynolds D.B, Repperger D.W, Phillips C.A, Bandry G (2003) Modeling the dynamic characteristics of pneumatic muscle. Annals of Biomedical Engineering, Springer, Vol. 31 : 310-317.

[13] Ariga Y, Pham H.T.T, Uemura M, Hirai H, Miyazaki F (2012) Novel Equilibrium-Point Control of Agonist-Antagonist System with Pneumatic Artificial Muscles. IEEE Int. Conf. on Robotics and Automation: 1470-1475.

[14] Fujimoto Y, Kominami T, Hamada H (2009) Development and Analysis of a High Thrust Force Direct-Drive Linear Actuator. IEEE Trans. on Industrial Electronics Vol. 56, No.5 : 1383-1392.

[15] Smadi I.A, Omori H, Fujimoto Y (2012) Development, Analysis and Experimental Realization of a Direct-Drive Helical Motor. IEEE Trans. On Ind. Electronics Vol. 59, No. 5 : 2208-2216.

[16] Yoshikawa T (1985) Manipulability of Robotic Mechanisms. Int Journal of Robotic Research, Vol. 4, No. 2 : 3-9.

[17] Ghorbel F.H, Chetelat O, Gunawardana R, Longchamp R (2000) Modelling and Set Point Control of Closed-Chain Mechanisms: Theory and Experiment. Int. Trans. on Control Systems Technology Vol. 8, no. 5 : 801-814.

[18] Murakami T, Yu F, Ohnishi K (1993) Torque Sensorless Control in Multidegree-of-freedom Manipulator. IEEE Trans. on Ind. Electronics Vol. 40, no. 2 : 259-265.

[19] Visioli A, Legnani G (2002) On the Trajectory Tracking Control of Industrial SCARA Robot Manipulators. IEEE Trans. on Ind. Electronics, Vol. 49, No. 1 : 224-232.

[20] An C. H, Atkeson C. G, Griffiths J. D, Hollerbach J. M (1989) Experimental Evaluation of Feedforward and Computed Torque Control. IEEE Trans. on Robotics and Automation Vol. 5, no. 3 : 368-373.

[21] Zhang Y.X, Chong S, Shang W.W, Li Z.X, Jiang S.L (2007) Modelling, Identification and Control of a Redundant Planar 2-DOF Parallel Manipulator. Int. Journal of Control, Automation and Systems Vol. 5, no. 5 : 559-569.

[22] Shukor A.Z, Fujimoto Y (2011) Workspace Control of Biarticular Manipulator. The IEEE Int. Conf. on Mechatronics : 415-420.

www.intechopen.com

Ahmad Zaki bin Hj Shukor and Yasutaka Fujimoto: 13
Planar Task Space Control of a Biarticular Manipulator Driven by Spiral Motors

[23] Shukor A.Z, Smadi I.A, Fujimoto Y (2011) Development of a Biarticular Manipulator using Spiral Motors. 37th Annual Conference on IEEE Industrial Electronics Society : 92-97.

[24] Spong M.W, Vidyasagar M (1989) Robot Dynamics and Control. John Wiley and Sons : 23-24.

[25] Ming Z. Huang (2011). Design of a Planar Parallel Robot for Optimal Workspace and Dexterity, International Journal of Advanced Robotic Systems, Vedran Kordic, Aleksandar Lazinica, Munir Merdan (Ed.), ISBN: 1729-8806, InTech, Available from: http://www.intechopen.com/journals/international_journal_of_advanced_robotic_systems/design_of_a_planar_parallel_robot_for_optimal_workspace_and_dexterity

[26] Shukor A.Z, Fujimoto Y (2012) Force Control of Musculoskeletal Manipulator. IEEE Int. Workshop on Advanced Motion Control (AMC), Paper ID. 74.